The null location is then moved along the uv plane and the optimized solutions of (9) are examined. Contours of the optimal objective function (9a) are shown in Fig. 4(a). At the various sidelobe locations of Fig. 3(a) the optimal objective takes a larger value, because a larger perturbation is required to produce a null. There exist locations $(\mathrm{u},\mathrm{v}) = (0.32,-0.62)$, $(\mathrm{u},\mathrm{v}) = (-0.68,0.38)$ and $(\mathrm{u},\mathrm{v}) = (0.32,-0.38)$ where the objective takes very large values. Such points are inherent to this optimization method, and are not due to the array dynamics [4]. As the optimal objective takes larger values, the solution eventually becomes unstable [see Fig. 4(a)]. The optimal objective can be reduced if the nulling constraint is relaxed by allowing a maximum level rather than a null. This is verified in Fig. 4(b), where the optimal objective function contours are displayed when a maximum level of -20 dB is desired instead. In addition, the regions of unstable solutions are greatly reduced.

V. Conclusion

The problem of constrained beam steering in planar coupled oscillator antenna arrays is formulated and solved as a convex optimization problem. Previous works on 1-D arrays are extended to describe the steady state and stability of planar arrays. The validity and limitations of the proposed method are demonstrated by a 7×7 array design example.

References

[1] S. Boyd and L. Vandenberghe, *Convex Optimization*. New York: Cambridge Univ. Press, 2004.

[2] T. Heath, "Simultaneous beam steering and null formation with coupled, nonlinear oscillator arrays," *IEEE Trans. Antennas Propag.*, vol. 53, no. 6, pp. 2031–2035, Jun. 2005.

[3] H. Steyskal, "Simple method for pattern nulling by phase perturbation," *IEEE Trans. Antennas Propag.*, vol. AP-31, no. 1, pp. 163–166, Jan. 1983.

[4] A. Georgiadis, A. Collado, and A. Suarez, "Pattern nulling in coupled oscillator antenna arrays," *IEEE Trans. Antennas Propag.*, vol. 55, no. 5, pp. 1267–1274, May 2007.

[5] Y. Nesterov and A. Nemirovskii, *Interior Point Polynomial Methods in Convex Programming*. Philadelphia, PA: SIAM, 1994, vol. 13, Studies in Applied Mathematics.

[6] I. Yamada, "The hybrid steepest descent method for the variational inequality problem over the intersection of fixed point sets of nonexpansive mappings," in *Inherently Parallel Algorithms in Feasibility and Optimization and Their Applications*, D. Butnariu, Y. Censor, and S. Reich, Eds. Amsterdam: Elsevier, 2001, pp. 473–504.

[7] Z.-Q. Luo and W. Yu, "An introduction to convex optimization for communications and signal processing," *IEEE J. Select. Areas Commun.*, vol. 24, no. 8, pp. 1426–1438, Aug. 2006.

TM Scattering From a Dielectric Biconvex Cylinder Loading a Shallow Circular Gap in a Perfectly Conducting Plane

Deng-How Tsaur and Kao-Hao Chang

***Abstract*—A series solution for TM scattering from a dielectric biconvex cylinder, which is formed by a semicircle and a portion of circular arc, buried in a shallow circular gap of a perfectly conducting plane is derived in this paper. The electric fields of biconvex cylinder region and its outer semi-unbounded region are represented in terms of an infinite series of cylindrical waves with unknown coefficients respectively. By employing Graf's addition theorem and matching the boundary conditions, the unknown coefficients are determined. The comparisons with available data in the literature point out a good agreement for the circular cylinder case. Some plotted results for the backscattering width and far-field radiation pattern reveal how the scattering properties have influenced by varying the depth-to-half-width ratio of the dielectric biconvex cylinder.**

***Index Terms*—Electromagnetic scattering, dielectric biconvex cylinder, shallow circular gap.**

I. Introduction

The scattering properties of the dielectric loads in a perfectly electric conducting (PEC) plane are of significant importance in many areas of technology such as antenna design, radar engineering, aircraft design, etc. In the past, the dielectric-loaded grooves of simple geometrical shapes in a PEC plane have been analyzed extensively; for example, a rectangular [1], V-shaped [2], semi-circular [3]–[5], semi-elliptic [6], trapezoidal groove [7] or a coaxial dielectric circular cylinder (DCC) loading in a semi-circular gap [8], etc.

In this paper, the authors aim to obtain a series solution for the TM wave scattering problem of a dielectric biconvex cylinder (DBC) loading a shallow circular gap in a PEC plane. A semicircle and a portion of circular arc form the DBC cross-section. When the depth-to-half-width ratio is unit, the DBC is just a circular one. In other words, the DCC is a special case of the DBC. To date, to the best of authors' knowledge, the case for DBC embedded in a shallow circular gap is not studied before.

II. Theoretical Formulation

The 2-D model depicted in Fig. 1 consists of a DBC buried in a shallow circular gap of a PEC plane. The interface S_I is a semicircle with radius a, while the boundary S_P is part of a circular arc with central angle 2β and radius a_1. The shallow circular gap is characterized by the depth-to-half-width ratio, d/a, which is related to the angle β by $d/a = \tan^{-1}(\beta/2)$. The wave numbers outside and inside the DBC are k_1 and $k_2 = k_1\sqrt{\varepsilon_r\mu_r}$, respectively, where ε_r and μ_r are relative permittivity and permeability, respectively. The definitions of two Cartesian and two cylindrical coordinate systems are taken as shown in Fig. 1. The vertical distance from the center of curvature of the gap to flat surface is e. The E-polarized plane waves of unit amplitude, which impinge upon the DBC at an angle α with respect to the positive x axis, are considered. The time-factor $\exp(j\omega t)$ is suppressed throughout.

Manuscript received October 5, 2006; revised March 5, 2007.

The authors are with the Department of Harbor and River Engineering, National Taiwan Ocean University, Keelung, 202 Taiwan, R.O.C. (e-mail: hretdh@mail.ntou.edu.tw).

Digital Object Identifier 10.1109/TAP.2007.905963

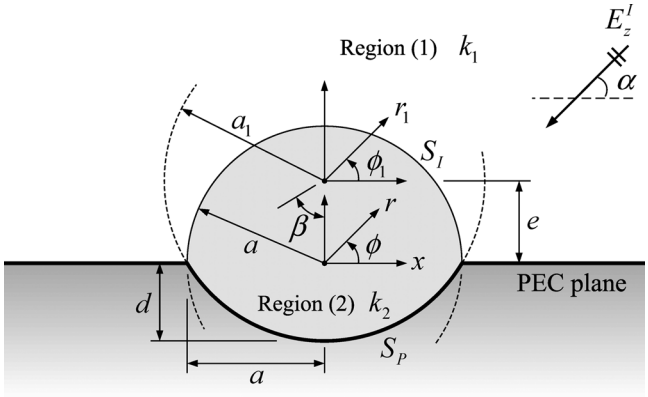

Fig. 1. Definition sketch for the problem.

As shown in Fig. 1, the analyzed domain is divided into two regions. In region (1) and (2), the electric field can be expressed as

$$E_z^{(1)}(r,\phi) = 4\sum_{n=1}^{\infty} j^n J_n(k_1 r)\sin n\alpha \sin n\phi + \sum_{n=1}^{\infty} A_n H_n^{(2)}(k_1 r)\sin n\phi \quad (1)$$

$$E_z^{(2)}(r,\phi) = \sum_{n=0}^{\infty} B_n J_n(k_2 r)\cos n\phi + \sum_{n=1}^{\infty} C_n J_n(k_2 r)\sin n\phi \quad (2)$$

where $k_1 = 2\pi/\lambda_1$, λ_1 is the free-space wavelength. $J_n(\cdot)$ is the Bessel function of the first kind of order n. $H_n^{(2)}(\cdot)$ is the Hankel function of the second kind of order n. The A_n, B_n, and C_n are the unknown expansion coefficients.

Enforcing continuity conditions across the semi-circular interface S_I and the boundary condition on the gap surface S_P with the aid of Graf's addition theorem [9], the following matrix form is obtained:

$$[Q_{vn}]\{B_n\} = \{R_v\} \quad (3)$$

where

$$Q_{vn} = F_{n,v}^{+} - \frac{2}{\pi}\sum_{u=1}^{\infty} F_{u,v}^{-}\frac{D_{n,u}}{D_{u,u}} I_{n,u}^{CS} \quad (4)$$

$$R_v = \frac{8}{\pi a}\sum_{n=1}^{\infty}\frac{j^{n+1}\sin n\alpha F_{n,v}^{-}}{D_{n,n}} \quad (5)$$

$$F_{n,q}^{+} = \sum_{m=0}^{\infty} J_m(k_2 a_1) \times \left[U_{m,n}^{+} I_{m,q}^{CS}(\beta) - V_{m,n}^{+} I_{m,q}^{SS}(\beta)\right] \quad (6)$$

$$F_{n,q}^{-} = \sum_{m=0}^{\infty} J_m(k_2 a_1) \times \left[-V_{m,n}^{-} I_{m,q}^{CS}(\beta) + U_{m,n}^{-} I_{m,q}^{SS}(\beta)\right] \quad (7)$$

$$I_{m,q}^{CS}(\beta) = \int_{-\pi/2-\beta}^{-\pi/2+\beta} \cos m\phi_1 \sin q\phi_1 d\phi_1 \quad (8)$$

$$I_{m,q}^{SS}(\beta) = \int_{-\pi/2-\beta}^{-\pi/2+\beta} \sin m\phi_1 \sin q\phi_1 d\phi_1 \quad (9)$$

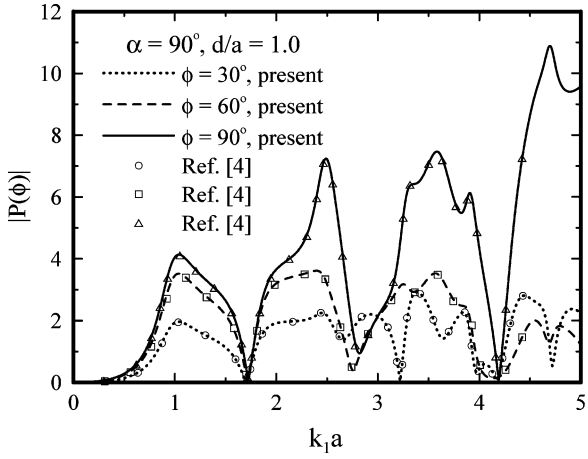

Fig. 2. Scattered field magnitude versus $k_1 a$ for a DCC.

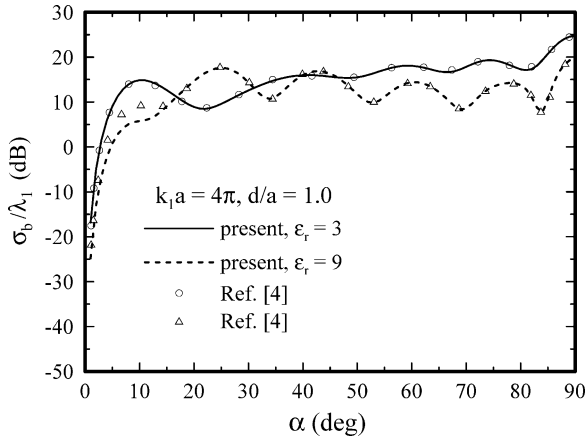

Fig. 3. Backscattering width versus α for a DCC.

$$I_{p,n}^{CS} = \int_0^{\pi} \cos p\phi \sin n\phi d\phi \quad (10)$$

$$U_{m,n}^{\pm} = \frac{\overline{\delta}_{0m}}{2}\left[(-1)^n J_{m-n}(k_2 e)\cos\left(\frac{m+n}{2}\right)\pi \pm J_{m+n}(k_2 e)\cos\left(\frac{m-n}{2}\right)\pi\right] \quad (11)$$

$$V_{m,n}^{\pm} = \frac{\overline{\delta}_{0m}}{2}\left[J_{m+n}(k_2 e)\sin\left(\frac{m-n}{2}\right)\pi \pm (-1)^n J_{m-n}(k_2 e)\sin\left(\frac{m+n}{2}\right)\pi\right] \quad (12)$$

$$D_{p,n} = J_p(k_2 a)H_n^{(2)\prime}(k_1 a) - J_p'(k_2 a)H_n^{(2)}(k_1 a) \quad (13)$$

in which $\overline{\delta}_{0n} = 2 - \delta_{0n}$, δ_{0n} is the Kronecker delta function and the prime means differentiation with respect to the argument.

Once the unknown coefficients B_n are obtained, the expansion coefficients A_n and C_n can be evaluated in a straightforward way.

III. Numerical Results and Discussion

A convergence test was done firstly to specify the truncation limit in the infinite series. It was worth emphasizing that the series in (6) and (7) should be accurately computed by numerically testing for their convergence to guarantee a given accuracy in (3), thereby leaving only one parameter in the numerical procedure, i.e., the terms of summation in (3). Following extensive numerical experiments 200 terms were chosen in (6) and (7) to produce the graphs in all cases. Numerical tests

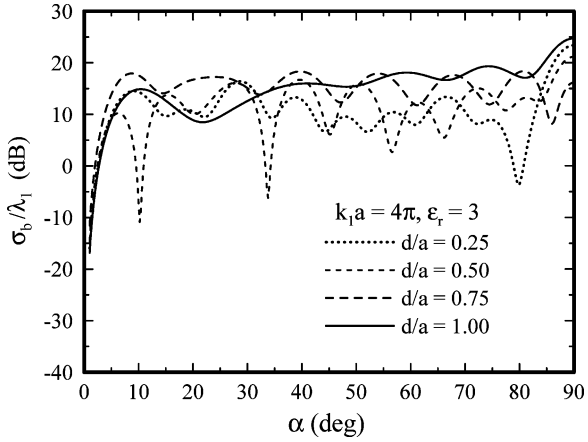

Fig. 4. Backscattering width versus α for a DBC with $\varepsilon_r = 3$.

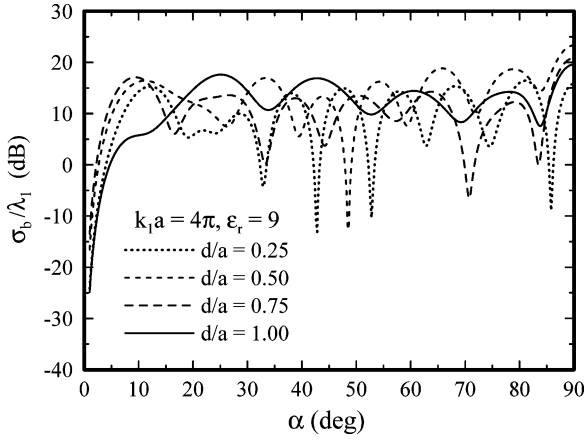

Fig. 5. Backscattering width versus α for a DBC with $\varepsilon_r = 9$.

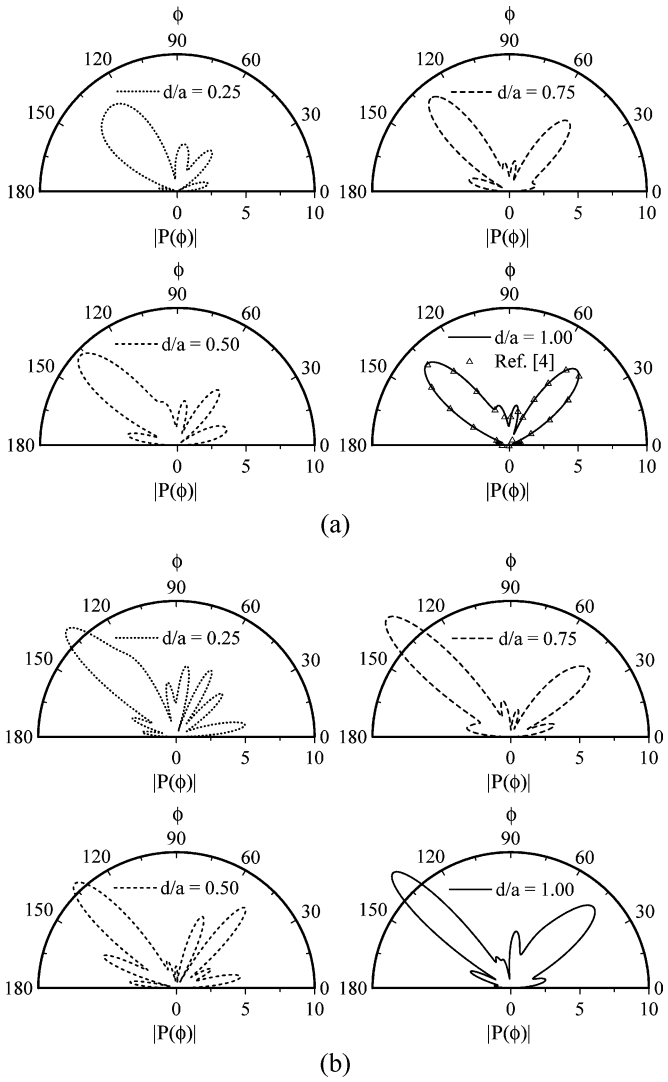

Fig. 6. Polar plots of scattered field magnitudes for different d/a. (a) $\alpha = 45^\circ$, $k_1 a = 7, k_2/k_1 = 15/7$; (b) $\alpha = 45^\circ$, $k_1 a = 11, k_2/k_1 = 15/7$.

also showed that more terms were required as the value of $k_1 a$ or ε_r increased.

The accuracy of the proposed series solution is checked against the DCC case $(d/a = 1.0)$ in [4]. In Fig. 2, the magnitude of far-field pattern $P(\phi)$ for scattering angle ϕ equal to 30°, 60°, and 90° at normal incidence $(\alpha = 90^\circ)$ is calculated and compared with [4, Fig. 4]. As it can be seen, the agreement is excellent.

To obtain further validation of the above formulation, the backscattering width σ_b versus incident angle α for a DCC case at $\varepsilon_r = 3$ and 9 is calculated. As shown in Fig. 3, the presented results are in good agreement with [4, Fig. 5].

To exhibit the effects of d/a of the DBC on the backscattering width at $k_1 a = 4\pi$ and $\varepsilon_r = 3$, the graph for different d/a is shown in Fig. 4. One may observe the strong effect on echo width pattern when the d/a changed. Fig. 5 is similar to Fig. 4 except that $\varepsilon_r = 9$. As seen in Fig. 5, a fast change in the echo width for smaller d/a is noticed.

The changes in the scattered field magnitudes with respect to the d/a of the DBC for $k_1 a = 7$ and 11 at $\alpha = 45^\circ$ are illustrated in Fig. 6. For the case of $d/a = 1$ in Fig. 6(a), the comparison between our result and that in [4, Fig. 6] is very well. Overall, one can see that the scattering pattern has a shape characteristic of high frequency scattering with an elongated main lobe at the forward direction.

IV. Conclusion

Based on the region-matching technique cooperating with Graf's addition theorem, a series solution has been presented for the problem of TM wave scattering from a DBC buried in a shallow circular gap of a PEC plane. The accuracy of the numerical results has been demonstrated through comparisons with a DCC case. The effects of d/a of the DBC on backscattering width and far-field radiation pattern were discussed. The model provided in this paper gives different biconvex shapes for the dielectric cylinder, thus the shapes of the dielectric cylinder will not be limited to a circle.

References

[1] K. Barkeshli and J. L. Volakis, "Scattering from narrow rectangular filled grooves," *IEEE Trans. Antennas Propag.*, vol. 39, no. 6, pp. 804–810, Jun. 1991.

[2] T. B. A. Senior, K. Sarabandi, and J. R. Natzke, "Scattering by a narrow gap," *IEEE Trans. Antennas Propag.*, vol. 38, no. 7, pp. 1102–1110, Jul. 1990.

[3] B. K. Sachdeva and R. A. Hurd, "Scattering by a dielectric-loaded trough in a conducting plane," *J. Appl. Phys.*, vol. 48, no. 4, pp. 1473–1476, Apr. 1977.

[4] T. J. Park, H. J. Eom, W. M. Boerner, and Y. Yamaguchi, "TM scattering from a dielectric-loaded semi-circular trough in a conducting plane," *IEICE Trans. Commun.*, vol. E75-B, no. 2, pp. 87–91, Feb. 1992.

[5] A. G. Tyzhnenko, "Two-dimensional TE-plane wave scattering by a dielectric-loaded semicircular trough in a ground plane," *Electromagn.*, vol. 24, pp. 357–368, 2004.

[6] W. J. Byun, J. W. Yu, and N. H. Myung, "TM scattering from hollow and dielectric-filled semielliptic channels with arbitrary eccentricity in a perfectly conducting plane," *IEEE Microw. Theory Tech.*, vol. 46, no. 9, pp. 1336–1339, Sep. 1998.
[7] V. P. Chumachenko, E. Karacuha, and M. Dumanli, "TM-scattering from a multiangular groove in a ground plane," *J. Electromagn. Waves Applicat.*, vol. 14, no. 3, pp. 329–347, 2000.
[8] H. A. Ragheb, "Electromagnetic scattering from a coaxial dielectric circular cylinder loading a semicircular gap in a ground plane," *IEEE Trans. Microw. Theory Tech.*, vol. 43, no. 6, pp. 1303–1309, Jun. 1995.
[9] G. N. Watson, *A Treatise on the Theory of Bessel Functions*, 2nd ed. Cambridge, U.K.: Cambridge Univ. Press, 1958.

Oblique Incidence Performance of a Novel Frequency Selective Surface Absorber

Ghaffer I. Kiani, Kenneth L. Ford, Karu P. Esselle, Andrew R. Weily, and Chinthana J. Panagamuwa

***Abstract*—Oblique incidence performance of a novel two-layer absorb/transmit frequency selective surface (FSS) is investigated. The FSS has good frequency stability for both horizontally and vertically polarized waves incident normally or at oblique angles. Due to its transmission for 900/1800/1900 MHz mobile bands and good absorption for 5 GHz waves, it has the potential as a security wall or isolator for 5 GHz WLAN systems. The absorption in the stop band helps reduce additional WLAN multipath fading caused by conventional reflecting FSS designs. The first layer of the FSS consists of conventional conducting cross dipoles having a circular aperture in the centre, while the second layer uses resistive cross dipoles. Moreover, the conducting cross dipoles have been sandwiched between two dielectric sheets to achieve a stable response for different angles of incidence. The periodicity of both FSS layers is the same while the distance between the two layers is reduced to one eighth of the free-space wavelength. This reduction leads to a more compact design compared to the conventional Salisbury screen, while still achieving acceptable absorption in the stopband. Both theoretical and experimental results are presented to confirm the performance of the absorb/transmit FSS.**

***Index Terms*—Absorber, delay spread, fading, frequency selective surface (FSS), multilayers, multipath, oblique incidence, security, two-layers, wireless networks, WLAN.**

I. Introduction

Frequency selective surfaces (FSSs) have been developed for use as spatial filters of microwaves and millimeter waves [1]. They have been considered for applications such as wireless security, radomes, antennas and telecommunications [2]. Common FSSs, which are reflect/transmit type, can be incorporated in the walls of buildings to provide wireless local area network (WLAN) security. They block WLAN signals while passing cellular phone signals [3] but give rise to heavy stopband reflections from the FSS surface causing additional delay spread and multipath fading in WLAN systems. Research has recently been undertaken to use lossy FSS as absorbers [4]–[6]. The main challenges in these designs are: a) to achieve stable response for oblique incidence for both polarizations (TE and TM); and b) to reduce the distance between the FSS and resistive sheets to achieve a compact design [4] without compromising absorption performance. Moreover, research has also been carried out to achieve stable frequency response for oblique angles from circuit analog absorbers at both parallel and perpendicular polarizations [7].

In this communication we present a novel absorb/transmit FSS designed to provide security and/or isolation for 5 GHz systems. It passes cellular phone signals and blocks 5 GHz signals by absorbing, as opposed to reflecting. The FSS is a two-layer structure, with conducting cross dipoles on one layer and resistive cross dipoles on the second layer. The advantages of the design are: 1) it provides absorption in 5 GHz band; 2) it maintains transmission of 900/1800/1900 MHz mobile phone bands; 3) the frequency of maximum attenuation remains relatively stable for different incident angles; and 4) it is more compact than conventional designs making it more practical for commercial use. These properties give the absorb/transmit FSS a clear advantage over conventional Salisbury and Jaumann absorbers, which typically can provide good absorption in the stopband but have poor out of band transmission.

In this design the frequency stability of both polarizations has been achieved by three techniques. Firstly, the inter-element spacing between cross dipoles has been reduced [1]. This improves its frequency response for oblique angles and has added considerable stability for both polarizations. Secondly, a small circular aperture has been etched at the centre of the conducting cross dipole to change its surface impedance. For a thin surface, the total electric field on the surface is equal to the product of the surface impedance and the surface current density, which can be represented as

$$\overrightarrow{E}^{\mathrm{inc}} + \overrightarrow{E}^{\mathrm{scat}} = Z_s \overrightarrow{J_s}$$

where Z_s is the surface impedance. The two limiting cases for this equation occur when $Z_s = 0$ or when Z_s approaches infinity. The boundary condition enforced by this equation is a PEC when $Z_s = 0$ (short-circuit). On the other hand if Z_s approaches infinity, the surface currents are forced to zero and hence no energy is scattered from the surface (open-circuit). In our cross dipole case, the open-circuit condition is approximated because removing patch from the center of the cross dipole increases the surface impedance [8]. The additional inductance due to narrow metal around the hole also contributes to tuning the FSS elements to resonate at 5 GHz. Thirdly, the conducting cross dipoles have been sandwiched between two dielectric layers to provide extra frequency stability and power handling [1]. There is no major improvement in the stability or the absorption of FSS absorber when the resistive cross dipole is sandwiched within two FR4 sheets.

II. Configuration

The unit cell configuration of the absorb/transmit FSS is shown in Figs. 1 and 2. The 5 GHz stopband filter characteristics are achieved by incorporating an array of conducting cross dipoles on one side of one of the FR4 sheets. Another sheet of FR4 with the same dielectric constant and thickness is placed on the open side of the array of conducting dipoles. This sandwiched configuration is shown in Fig. 1. The absorption around 5 GHz is achieved by incorporating a layer of

Manuscript received March 15, 2007; revised May 11, 2007. This work was supported in part by Macquarie University, Sydney, Australia, and in part by the University of Sheffield.

G. I. Kiani and K. P. Esselle are with the Department of Electronic Engineering, Macquarie University, Sydney, New South Wales 2109, Australia (e-mail: gkiani@ics.mq.edu.au).

K. L. Ford is with the Department of Electronic and Electrical Engineering, University of Sheffield, Sheffield S1 3JD, U.K.

A. R. Weily is with CSIRO ICT Centre, Epping, New South Wales 1710, Australia.

C. J. Panagamuwa is with the Department of Electronic and Electrical Engineering, Loughborough University, Loughborough LE11 3TU, U.K.

Digital Object Identifier 10.1109/TAP.2007.905980